

## Influence of indenter shape on nanoindentation: an atomistic study

Chia-Wei Lai and Chuin-Shan Chen\*

*Department of Civil Engineering, National Taiwan University, Taipei, Taiwan*

(Received August 20, 2013, Revised September 5, 2013, Accepted September 16, 2013)

**Abstract.** The influence of indenter geometry on nanoindentation was studied using a static molecular dynamics simulation. Dislocation nucleation, dislocation locks, and dislocation movements during nanoindentation into Al (001) were studied. Spherical, rectangular, and Berkovich indenters were modeled to study the material behaviors and dislocation activities induced by their different shapes. We found that the elastic responses for the three cases agreed well with those predicted from elastic contact theory. Complicated stress fields were generated by the rectangular and Berkovich indenters, leading to a few uncommon nucleation and dislocation processes. The calculated mean critical resolved shear stresses for the Berkovich and rectangular indenters were lower than the theoretical strength. In the Berkovich indenter case, an amorphous region was observed directly below the indenter tip. In the rectangular indenter case, we observed that some dislocation loops nucleated on the plane. Furthermore, a prismatic loop originating from inside the material glided upward to create a mesa on the indenting surface. We observed an unusual softening phenomenon in the rectangular indenter case and proposed that heterogeneously nucleating dislocations are responsible for this.

**Keywords:** nanoindentation; indenter shape; berkovich indenter; dislocation; heterogeneous nucleation; molecular dynamics

### 1. Introduction

Advances in nanoindentation techniques have greatly enabled researchers to probe and investigate material properties at the nanometer scale. Nanoindentation testing is now a ubiquitous tool for the characterization of the mechanical properties of materials at the nanometer scale (Fischer-Cripps 2011). The properties of small volumes of materials probed by nanoindentation testing are usually different from their macroscopic counterparts and different deformation mechanisms are generally thought to be a significant contribution to this discrepancy (Kiely and Houston 1998).

With recent advances in computing power, researchers have adopted atomistic simulations to probe and understand detailed deformation processes and the mechanisms involved in nanoindentation (Lilleodden *et al.* 2003, Lee *et al.* 2005, Chen *et al.* 2008, Chan *et al.* 2011). Lilleodden *et al.* (2003) carried out an atomistic study of Au nanoindentation and reported the

---

\*Corresponding author, Professor, E-mail: dchen@ntu.edu.tw

elastic anisotropy of Au metal. They also studied the influence of indenter compliance on their nanoindentation results and concluded that stiffer indenters reduce the critical load and displacement for dislocation nucleation. Lee *et al.* (2005) carried out several atomistic studies on Al nanoindentation and reported that the critical resolved shear stress (a continuum-based indicator) is no longer a valid criterion in predicting dislocation nucleation. Chen *et al.* (2008) studied dislocation structures, mean contact pressure, and the nanohardness of Au and Al thin films using atomistic simulations. Two different characteristics were found in the induced dislocation structures: widespread slip activities in Al and confined and intact structures in Au. For both samples, the mean contact pressure varied significantly during the early stages of indentation but reached a steady value soon after the first apparent load drop. Chan *et al.* (2011) studied the size effects of nanoindentation using atomistic simulations. For spherical indenters with radii ranging from 10 to 50 Å, it was found that nanohardness was inversely proportional to the indenter radius. For Berkovich indenters, it was found that nanohardness and indentation depth were roughly inversely proportional.

In this study, we aim to examine how the development of dislocation microstructures is affected by complex stress states from different shapes of indenters. A spherical indenter, a rectangular indenter, and a Berkovich indenter are employed. Elastic behavior from an atomistic simulation is compared with solutions from elastic contact theory. Dislocation nucleation, dislocation locks, and dislocation movements during nanoindentation of Al (001) are studied in detail.

## 2. Methodology

The purpose of this atomistic study is to investigate the influences of indenter geometry on Al(001) nanoindentation. Three indenters with different geometries are employed: spherical, rectangular, and Berkovich indenters. Fig. 1 shows two-dimensional representations of the three indenters. They are modeled by atoms arranged in a cubic lattice and are treated as rigid bodies. The indenter–surface interaction is modeled by a purely repulsive interaction (Chen *et al.* 2008)

$$V(r) = \varepsilon(r/\rho)^{-12} \quad (1)$$

where  $r$  is the distance from an indenter atom to a surface atom. The parameters  $\varepsilon = 25$  meV and  $\rho = 3$  Å are used in this study.

The Al(001) atomistic configurations are modeled using three simulated cells of dimensions  $320 \times 276 \times 195$  Å (each contains roughly 1 million atoms) and they are oriented such that the [100], [010], and [001] crystallographic directions are parallel to the X, Y, and Z directions, respectively. Periodic boundary conditions are imposed along the X and Y directions and fixed boundary conditions are applied to the bottoms of the samples. The embedded-atom method potential proposed by Ercolessi and Adams (1994) is employed to model the atomic systems of the Al metal. Nanoindentation is performed by driving the indenter into the simulated sample along the Z direction using small steps (0.05 to 0.1 Å). At each step, the new stable equilibrium configuration is obtained using the Polak–Ribiere variation of the conjugate gradient method (Press *et al.* 2000).

A slip vector is employed to identify defect structures (Zimmerman *et al.* 2001). The slip vector of atom  $\alpha$  is

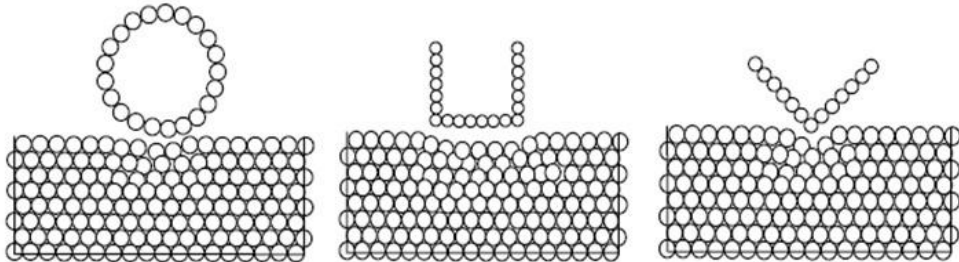


Fig. 1 Schematic representations of the three different indenters (from left to right: spherical indenter, rectangular indenter, and Berkovich indenter)

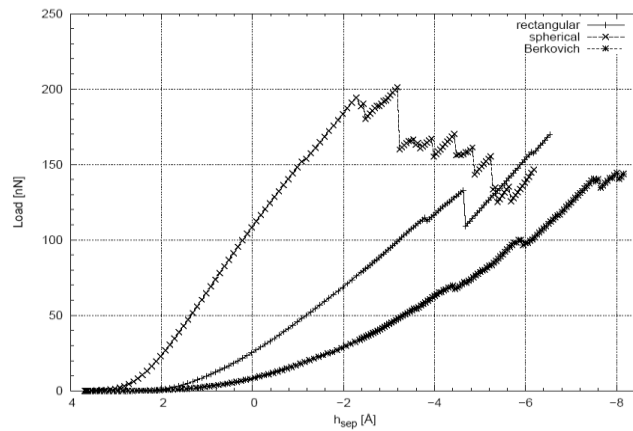


Fig. 2 Load–displacement curves for the three indenters

$$s^\alpha = -\frac{1}{n_s} \sum_\beta (\mathbf{r}^{\alpha\beta} - \mathbf{R}^{\alpha\beta}) \quad (2)$$

where the index  $\beta$  accounts for the nearest neighbors of atom  $\alpha$ ,  $n_s$  is the number of slipped neighbors of atom  $\alpha$ , and  $\mathbf{r}^{\alpha\beta}$  and  $\mathbf{R}^{\alpha\beta}$  are the vector differences between atom  $\alpha$  and atom  $\beta$  in the current and initial states, respectively. In this study, the initial state is set to be the zero-mechanical-stress state immediately prior to nanoindentation and the current state is the state of interest.

### 3. Results and discussion

#### 3.1 Elastic regime

In this section, efforts will be dedicated to the elastic responses of the nanoindentation simulations. A comparative study between the calculated results and the analytical models for the corresponding geometrically different indenters is carried out.

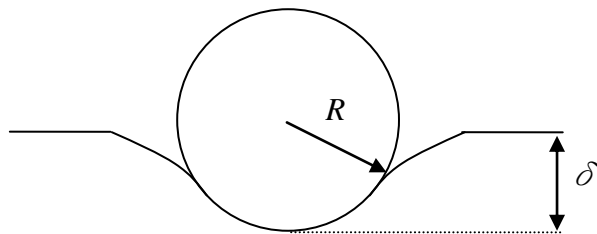


Fig. 3 Geometry of the contact problem for a spherical indenter

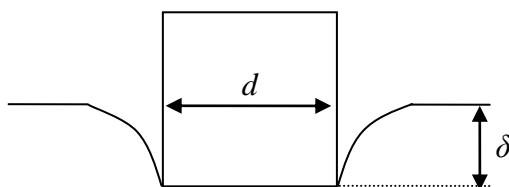


Fig. 4 Geometry of the contact problem for a rectangular indenter

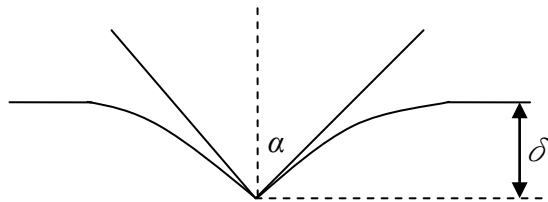


Fig. 5 Geometry of the contact problem for a conical indenter

A schematic representation of a spherical indenter contacting an infinite flat surface is shown in Fig. 3. For a rigid spherical indenter, the relationship between the indentation load ( $P$ ) and the indentation depth ( $\delta$ ) is given by (Fischer-Cripps 2011)

$$P = \frac{4}{3} R^{1/2} \delta^{3/2} \frac{E_s}{1 - \nu_s^2} \quad (3)$$

where  $R$  is the radius of the spherical indenter, and  $\nu_s$  and  $E_s$  are Poisson's ratio and Young's modulus of the material sample, respectively.

A schematic representation of a rectangular indenter contacting an infinite flat surface is shown in Fig. 4. In this study, a rigid square punch indenter, which is a special case of a rectangular indenter, is employed. For a rigid square punch indenter, the relationship between the indentation load ( $P$ ) and the indentation depth ( $\delta$ ) is given by (Bosakov 2003)

$$P = 2.292 \cdot \frac{d}{2} \cdot \delta \cdot \frac{E_s}{1 - \nu_s^2} \quad (4)$$

where  $d$  is the dimension of the square indenter.

A schematic representation for a conical indenter contacting an infinite flat surface is shown in Fig. 5. A rigid Berkovich indenter is equivalent to a rigid conical indenter with an effective semi-angle,  $\alpha$ , of  $70.30^\circ$  (Fischer-Cripps 2011). Therefore, for a rigid Berkovich indenter, the relationship between the indentation load ( $P$ ) and the indentation depth ( $\delta$ ) can be approximated by that of a rigid conical indenter of  $\alpha = 70.30^\circ$  (Bosakov 2003)

$$P = \frac{2 \tan 70.30}{\pi} \cdot \delta^2 \cdot \frac{E_s}{1 - \nu_s^2} \quad (5)$$

Using the above expressions for  $P(\delta)$ , one can calculate the elastic behaviors for the three indenters if the elastic properties of the material samples are known. In this study, the indenting direction is [001]. The isotropic elastic constants of Al given by Ercolelli and Adams (1994) are inadequate because we want to extract the elastic response along the [001] direction only. That is, the anisotropy of the system must be taken into account. Hosford (1993) proposed that the Young's modulus along a direction,  $\mathbf{d}$ , of a cubic crystal system,  $E_d$ , is

$$\frac{1}{E_d} = s_{11} + \frac{(2s_{12} - 2s_{11} + s_{44})(k^2l^2 + l^2h^2 + h^2k^2)}{(h^2 + k^2 + l^2)^2} \quad (6a)$$

where  $\mathbf{d}$  is expressed by direction indices  $[hkl]$ , and  $s_{11}$ ,  $s_{12}$ , and  $s_{44}$  are

$$\left. \begin{aligned} s_{11} &= \frac{c_{11} + c_{12}}{c_{11}^2 + c_{11}c_{12} - 2c_{12}^2} \\ s_{12} &= \frac{-c_{12}}{c_{11}^2 + c_{11}c_{12} - 2c_{12}^2} \\ s_{44} &= \frac{1}{c_{44}} \end{aligned} \right\} \quad (6b)$$

where  $c_{11}$ ,  $c_{12}$ , and  $c_{44}$  are elastic moduli for a cubic crystal system, and, in this study, they equal 118 GPa, 62.4 GPa, and 32.5 GPa, respectively (Ercolelli and Adams 1994). Therefore, we calculate the Young's modulus along the [001] direction,  $E_{001}$ , to be 75.07 GPa. By performing a Voigt average on the cubic crystal, we can also obtain the expression for Poisson's ratio

$$\nu_s = \frac{1}{2} \left( \frac{C_{11} + 4C_{12} - 2C_{44}}{2C_{11} + 3C_{12} + C_{44}} \right) \quad (7)$$

and  $\nu_s = 0.3196$ .

Before a direct comparison between the simulation results and theoretical predictions can be made, the results of the nanoindentation simulations need to be modified. Note that the

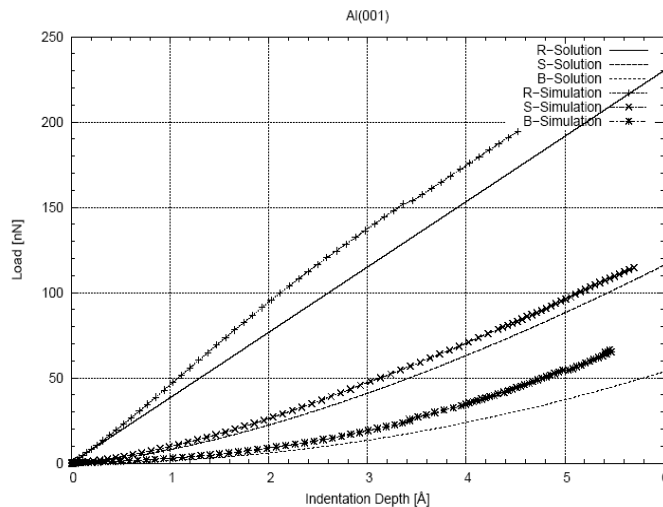


Fig. 6 Load-indentation depth curves of the elastic predictions and of the atomistic simulation results

displacement,  $h_{\text{sep}}$ , in Fig. 2 is defined as the separation distance between the indenter apex and the surface before nanoindentation and is not the indentation depth,  $\delta$ , which is defined as the maximum penetration depth from the original surface before nanoindentation. Therefore, the recovery process from the true indentation depth for the simulation results must be considered. For each simulation case, we process all the configurations before the first defect nucleation is observed, and for each configuration, we find all “position displacements” of the top-layer atoms on the indented surface and set the maximum “position displacement” as the indentation depth for each configuration. The “position displacement” for each atom is defined as the Z coordinate difference between the same atom in the initial configuration (before indentation occurs) and the current configuration. Since the material sample is deformed elastically in the elastic regime, this strategy for modeling the recovery can reasonably retrieve the true indentation depths for each configuration.

Fig. 6 shows the simulated data after recovering the true indentation depth along with the curves of the elastic predictions for the three indenters. The curves predicted using the atomistic simulation and the elastic contact theory agree quite well. However, the trends predicted by the elastic theory and the atomistic simulation results for the Berkovich indenter gradually diverge. We are convinced that the insufficient equivalence between the rigid conical indenter and the rigid Berkovich indenter is responsible for this discrepancy.

### 3.2 Incipient plasticity

The load-displacement curves for the three indenters are examined in detail in the following section. All significant data points are denoted with unique labels in Figs. 7-9.

#### 3.2.1 Spherical indenter

Fig. 7 shows the curve for Al(001) indented with a spherical indenter. All significant data points are denoted with unique labels from s1 to s3. Three inflection points, signifying yielding

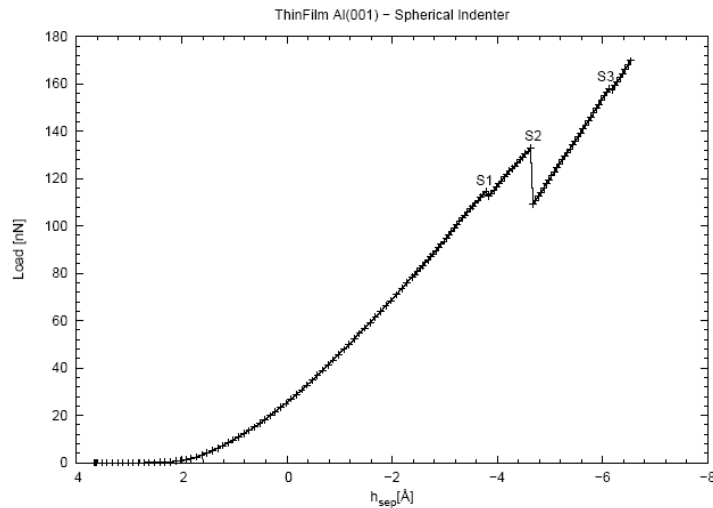


Fig. 7 Load–displacement curves for spherical indenter

events at the indentation site, are identified in the curve. Between inflection points, the curve exhibits a stable quasi-elastic behavior.

The indenter force field begins to contact the aluminum sample when the separation is 3.658 Å, and, subsequently, the internal stress steadily increases resulting in an increase in the curve. Before the first inflection point, s1, no defect structure is observed, which implies that the aluminum sample is elastically deformed. At s1 ( $h_{\text{sep}} \approx -3.532$  Å; the negative sign denotes that the indenter is below the level of the original surface), and dislocation processes begin to take place. A twofold rotation-symmetric (the rotation axis coincides with the Z axis) dislocation structure nucleates directly below the region in contact with the indenter. The curve suffers a small load drop of about 2 nN. Between s1 and s2, the curve ascends smoothly and shows a quasi-elastic behavior.

At s2 ( $h_{\text{sep}} \approx -4.632$  Å), a relatively large load drop occurs. The drop corresponds to a 24 nN decrease in the indentation load. A dramatic change of the dislocation structure under the indentation site is responsible for this load degeneration. The original twofold rotation-symmetric dislocation structure is transformed into a prismatic dislocation loop that immediately descends into the aluminum sample. This prismatic loop is stopped by the atoms at the bottom of the aluminum sample, upon which a fixed boundary is exerted. The back stress exerted by the piled-up prismatic loop causes the indentation load to accumulate again. The curve again exhibits a quasi-elastic behavior on its way to s3 ( $h_{\text{sep}} \approx -6.132$  Å).

The Hardy stress tensor (Tadmor and Miller 2010) is employed to analyze the stress state in a rectangular deformed region, which is located directly below the indentation site. The size of the region is set to a volume that contains a significant amount of dislocation defects. The bond length fraction used in the Hardy definition is set to 1, since the calculation of the bond length fraction is too complicated for a rectangular geometry. We are convinced that, as long as the averaging volume is large enough, the stress tensor obtained should approach the original definition. The calculated mean critical resolved shear stress ranges from 3.84 GPa to 3.34 GPa, which is close to the theoretical shear strength of this aluminum potential,  $\frac{\mu}{2\pi} = 5.28$  GPa (Zimmerman *et al.* 2001).

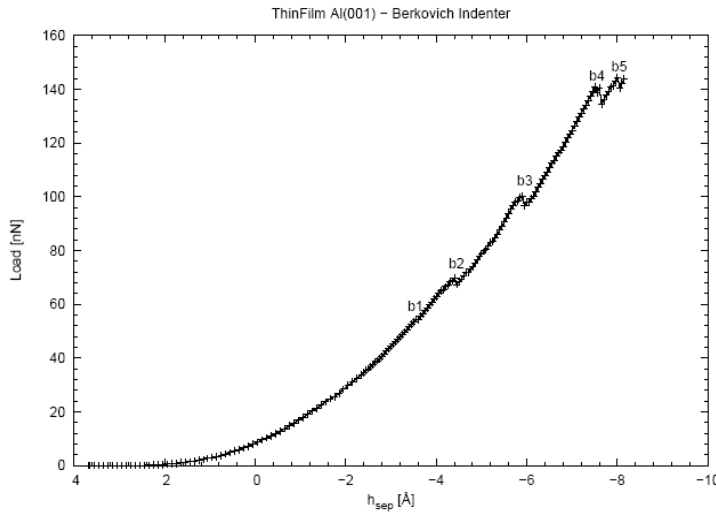


Fig. 8 Load–displacement curves for the Berkovich indenter

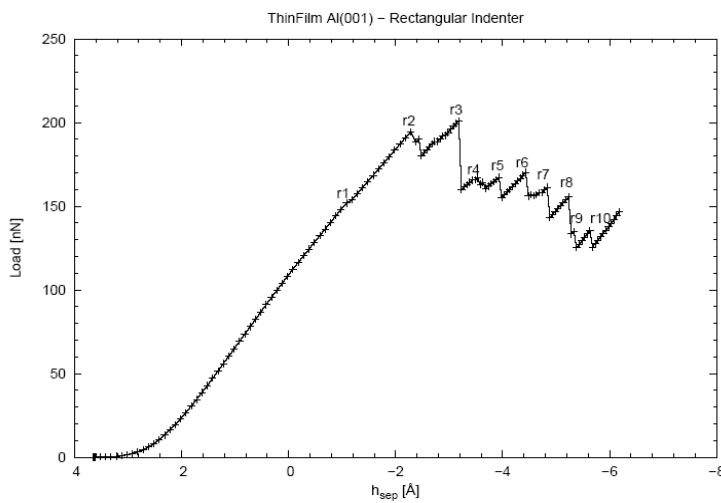


Fig. 9 Load–displacement curves for the rectangular indenter.

### 3.2.2 Berkovich indenter

The load–displacement curve for the Berkovich indenter is shown in Fig. 8 and five inflection points are presented. Similar to the spherical indenter case, quasi-elastic behaviors are observed between inflection points. Nevertheless, in comparison with the spherical indenter case, the load drop events tend to be small or not noticeable. Fig. 11 shows the evolution of the dislocation structure under the indentation site.

The indentation begins at  $3.658 \text{ \AA}$  when the indenter force field contacts the simulated sample. Unlike the spherical indenter case, a tetrahedral-shaped region containing atoms of relatively large displacements is observed before the first dislocation nucleation event at  $b_1$  ( $h_{sep} \approx -3.552 \text{ \AA}$ ). The region begins to grow when the separation is approximately  $-2.0 \text{ \AA}$ . However, no dislocation can

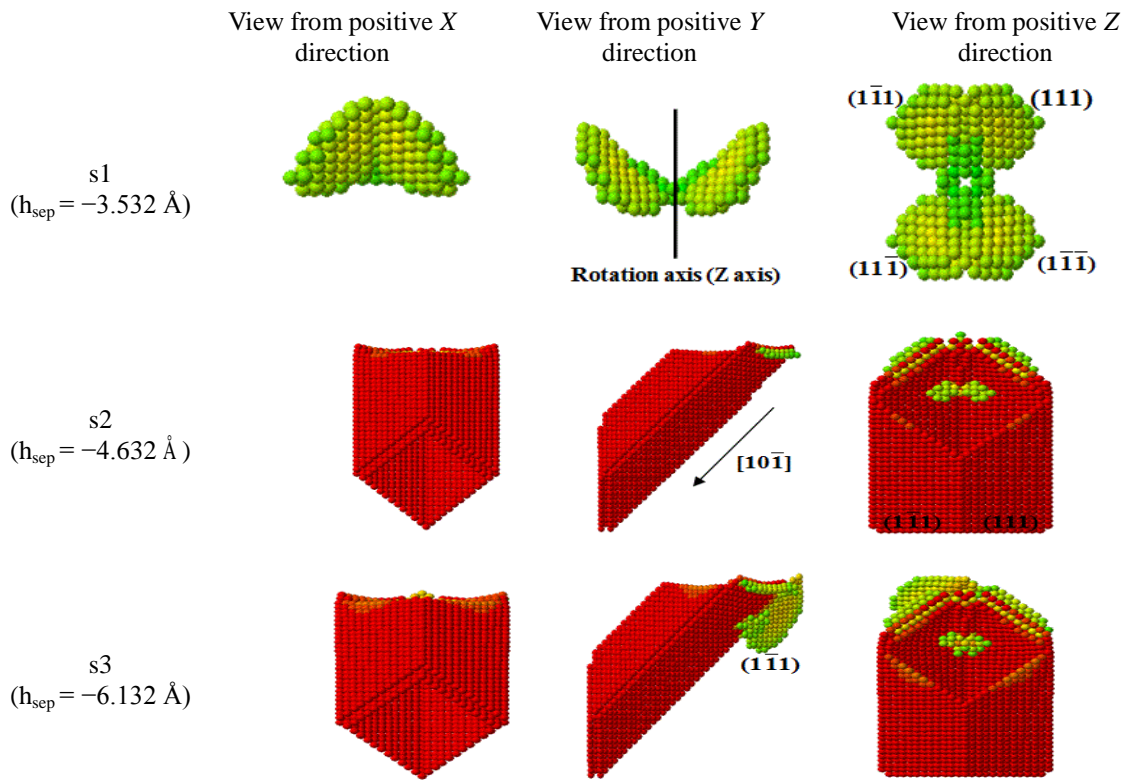


Fig. 10 Evolution of defect structures for the spherical indenter case.

be identified from this tetrahedral-shaped region, and it appears that the presence of the region does not significantly affect the load–displacement curve. The curve still behaves nearly elastically until the first dislocation nucleation event.

At b1, the curve suffers a very small load drop of approximately 0.016 nN. Dislocation nucleates at one of the four corners of the tetrahedral-shaped region. The dislocation continues to grow as the indenter is punched deeper into the sample. At b2 ( $h_{\text{sep}} \approx -4.452 \text{ \AA}$ ), a dislocation cross-slip event occurs, corresponding to a load drop of approximately 2.482 nN. At b3 ( $h_{\text{sep}} \approx -5.902 \text{ \AA}$ ), a load drop of approximately 3.39 nN occurs. More dislocation loops are activated at this point. After b3, a dislocation lock formation and a stacking fault region extension are observed. The curve rises until another obvious load drop occurs at b4 ( $h_{\text{sep}} \approx -7.602 \text{ \AA}$ ), where a new dislocation loop nucleates. This nucleation corresponds to a load drop of approximately 5.972 nN. Before the simulation ends, another load drop of approximately 4.178 nN occurs at b5 ( $h_{\text{sep}} \approx -8.002 \text{ \AA}$ ). This causes a slight change to the original defect structure.

By employing Hardy stress definition, we calculate the mean critical resolved shear stress to be in the range 2.5 GPa to 1.83 GPa. Compared to the values measured in the spherical case (3.84 GPa to 3.34 GPa), the mean critical resolved shear stress is much lower. This may be due to the presence of the tetrahedral-shaped defect region, which serves as an inhomogeneity in the aluminum sample. Zimmerman *et al.* (2001), Li *et al.* (2002) indicated that inhomogeneities present in the material sample could greatly reduce the dislocation nucleation stress in

nanoindentation experiments. The tetrahedral-shaped defect region appearing before the first dislocation nucleation introduces an inhomogeneity into the aluminum sample. Consequently, the observed mean critical resolved shear stress is far below the values of the spherical case, in which no inhomogeneity before the first dislocation nucleation is observed.

### 3.2.3 Rectangular indenter

Compared to the other two cases, the load–displacement curve for the rectangular indenter in Fig. 9 presents more inflection points. Although quasi-elastic behaviors are observed between the inflection points, they do not last as long in increasing load periods. Fig. 11 presents a series of transitions of the dislocation structures under the indentation site.

The indenter force field and the aluminum sample begin to be in contact when the separation  $3.658 \text{ \AA}$ . Then the curve smoothly increases until the first defect nucleation at r1 ( $h_{\text{sep}} \approx -1.082 \text{ \AA}$ ). Instead of a load drop, this nucleation manifests as a sudden change in the slope of the curve. This corresponds to three dislocation leaves originating from three out of the four corners of the rectangular indentation. Under the inactive corner, instead of a dislocation loop, only atoms with relatively large displacements are observed. At r2 ( $h_{\text{sep}} \approx -2.282 \text{ \AA}$ ), the first load drop event occurs. The dislocation leaves nucleating at r1 grow into the aluminum sample and interact with each other to form dislocation locks.

At r3 ( $h_{\text{sep}} \approx -3.182 \text{ \AA}$ ), the dislocation structure under the indentation site experiences a dramatic change. A dislocation leave appears from under the originally inactive corner and grows to form dislocation locks with other already-existing dislocation leaves. This dramatic change in the dislocation structure causes a relatively large load drop of approximately 41.3 nN.

At r4 ( $h_{\text{sep}} \approx -3.532 \text{ \AA}$ ), a load drop of approximately 3.7 nN occurs, and at r5 ( $h_{\text{sep}} \approx -3.932 \text{ \AA}$ ), a load drop of approximately 12 nN occurs. This corresponds to a dislocation double cross-slip event. At r6 ( $h_{\text{sep}} \approx -4.432 \text{ \AA}$ ), three dislocation cross-slip events are observed and the drop in indentation load is approximately 14 nN.

At r7 ( $h_{\text{sep}} \approx -4.832 \text{ \AA}$ ), a tetrahedral-shaped dislocation structure is formed. The load drop to accommodate this structure transition is approximately 18 nN. At r8 and r9, the dislocation structure does not change much, and corresponds to load drops of approximately 22 nN and 9.5 nN, respectively. At r10, a prismatic dislocation loop nucleates inside the aluminum sample. This loop glides upward toward the surface and forms a mesa with a height of approximately  $1.814 \text{ \AA}$ . This event causes the indentation load to drop approximately 9.7 nN.

As shown in Fig. 9, the curve starts to trend downward after r3, which suggests that little work hardening occurs. However, the general belief is that dislocation reactions and lock formations will harden the material sample during an indentation experiment (Hirth and Lothe 1982). In our case, we observed prolific dislocation activities, including dislocation reactions, lock formations, and dislocation double cross-slip events. However, work hardening is absent.

To explain this phenomenon, we analyze the local stress under the indentation site during the indentation experiment. The calculated mean critical resolved shear stress at r1 ranges from 3.84 GPa to 3.33 GPa, which agrees with the spherical indenter case very well. However, we find that, after r1, the dislocation nucleation stress begins to degenerate. That is, dislocations nucleate at lower stress levels. Vliet *et al.* (2003) suggest that dislocations nucleate from heterogeneous dislocation sources, such as Frank–Read sources, at much lower stress levels than those that nucleate from a perfect crystal (homogeneous nucleation). In this case, the dislocation interactions under the indentation site are prolific and complex, which leads to the embedding of heterogeneous dislocation sources in the material sample. These introduced heterogeneous

dislocation sources give rise to the degeneration of dislocation nucleation stress, and hence result in the reduced work-hardening phenomenon.

### 3.3 Microstructure evolution

In the following section, atoms of magnitude  $|s^\alpha|$  ranging from 0.1 to 4.0 are identified and colored according to the magnitude of the slip vector.

#### 3.3.1 Spherical indenter

The first defect nucleation appears at s1 in Fig. 7, which suggests that the material sample deforms elastically prior to this. At s1, a twofold rotation-symmetric dislocation structure nucleates directly below the indenter contact region. As Fig. 10 at s1 shows, the four leaves of this dislocation structure all nucleate on the  $\{111\}$  planes, which are the favored slip planes in a face-centered cubic (FCC) crystal. Each leave corresponds to a dislocation loop. The four leaves maintain their shapes and continue to grow as the external loading increases.

Between s1 and s2, the load–displacement curve rise quasi-elastically, which can be attributed to the external stress exerted by the indenter and the back stress induced by the dislocation loops achieving dynamic equilibrium. At s2, the twofold rotation-symmetric dislocation structure disappears, and a prismatic dislocation loop is observed instead. From the indentation site, the prismatic dislocation loop glides downward along  $[10\bar{1}]$  and leaves a trace behind it on two sets of the  $(1\bar{1}1)$  and  $(11\bar{1})$  slip planes. The nucleation of this prismatic dislocation loop manifests itself in the load–displacement curve as a considerable load drop of approximately 24 nN.

After this load drop, the curve increases again until another load drop occurs at s3. Between #s2 and #s3, the curve again behaves quasi-elastically and the defect structure in this period does not change significantly. At s3, a new dislocation loop nucleates on the  $(1\bar{1}1)$  plane.

The simulation finally stops at  $h_{sep} \approx -6.53 \text{ \AA}$ . Throughout this simulation, the often-reported dislocation locks are not identified. All dislocations nucleate on the favored slip planes,  $\{111\}$ , which agrees with the prediction from dislocation theory (Hirth and Lothe 1982).

#### 3.3.2 Berkovich indenter

As Fig. 11 at b1 shows, a dislocation loop nucleates from the site marked by a black circle. Besides the dislocation loop, a tetrahedral-shaped defect region is also observed. As the indentation continues, the dislocation loops and the defect region grow. At b2, a dislocation cross-slip event occurs. A dislocation loop originally situated on the  $(1\bar{1}\bar{1})$  plane cross-slips to the  $(11\bar{1})$  plane. At b3, a dislocation originally situated on  $(11\bar{1})$  shrinks and disappears while another dislocation loop begins to grow on  $(1\bar{1}\bar{1})$ . Dislocation shrinking was also observed by Liang *et al.* (2004), and results from the local stress variation. At b4, the size of the dislocation structure is much larger than it was at b3, but the shape does not change significantly. At b5, a new dislocation loop nucleates on  $(11\bar{1})$ . Throughout the simulation, all dislocation loops are observed to originate from one of the three corners of the triangular indentation marked by a black circle at b5 in Fig. 11. The asymmetric stress field induced by the Berkovich indenter is likely to be responsible for this asymmetric nucleation.

It is worth noting that a tetrahedral defect region is observed in this case. It may be caused by the extremely singular stress field resulting from the very sharp tip of the Berkovich indenter. This extremely singular stress field causes the atoms near the tip to quickly rearrange themselves in a process dissimilar to slipping, or may even “break” the bonds between them.

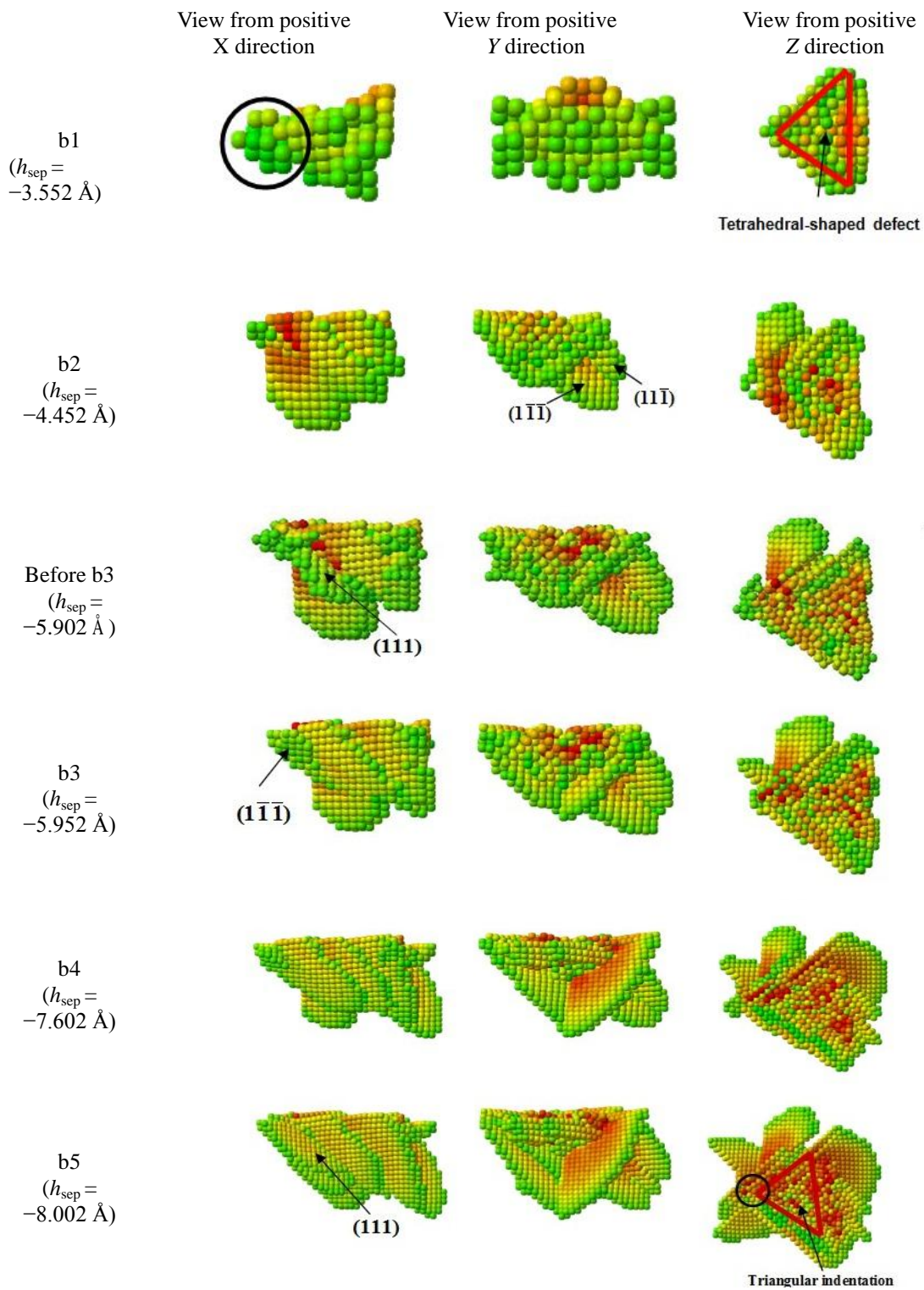


Fig. 11 Evolution of defect structures for the Berkovich indenter case

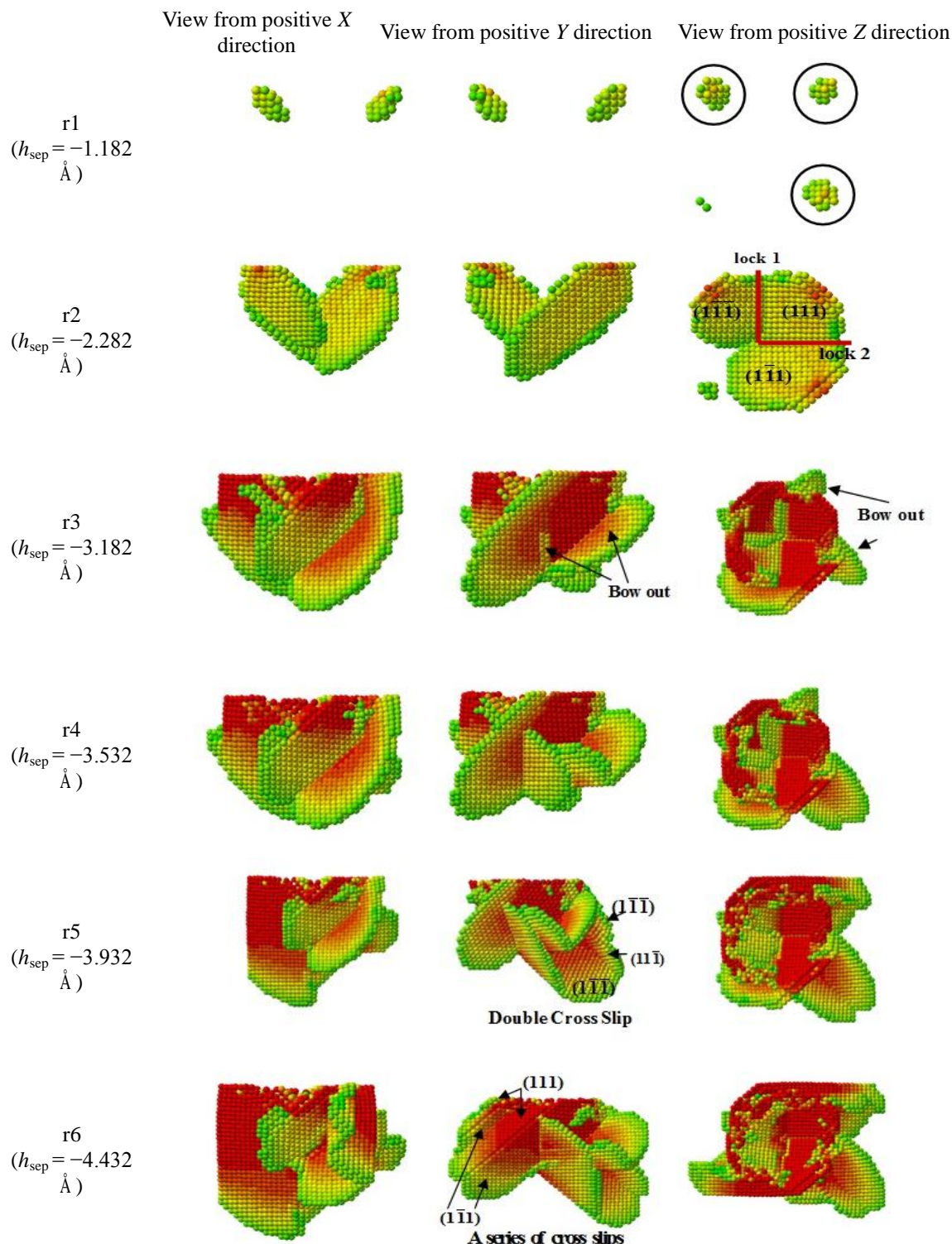


Fig. 12 Evolution of defect structures for the rectangular indenter case

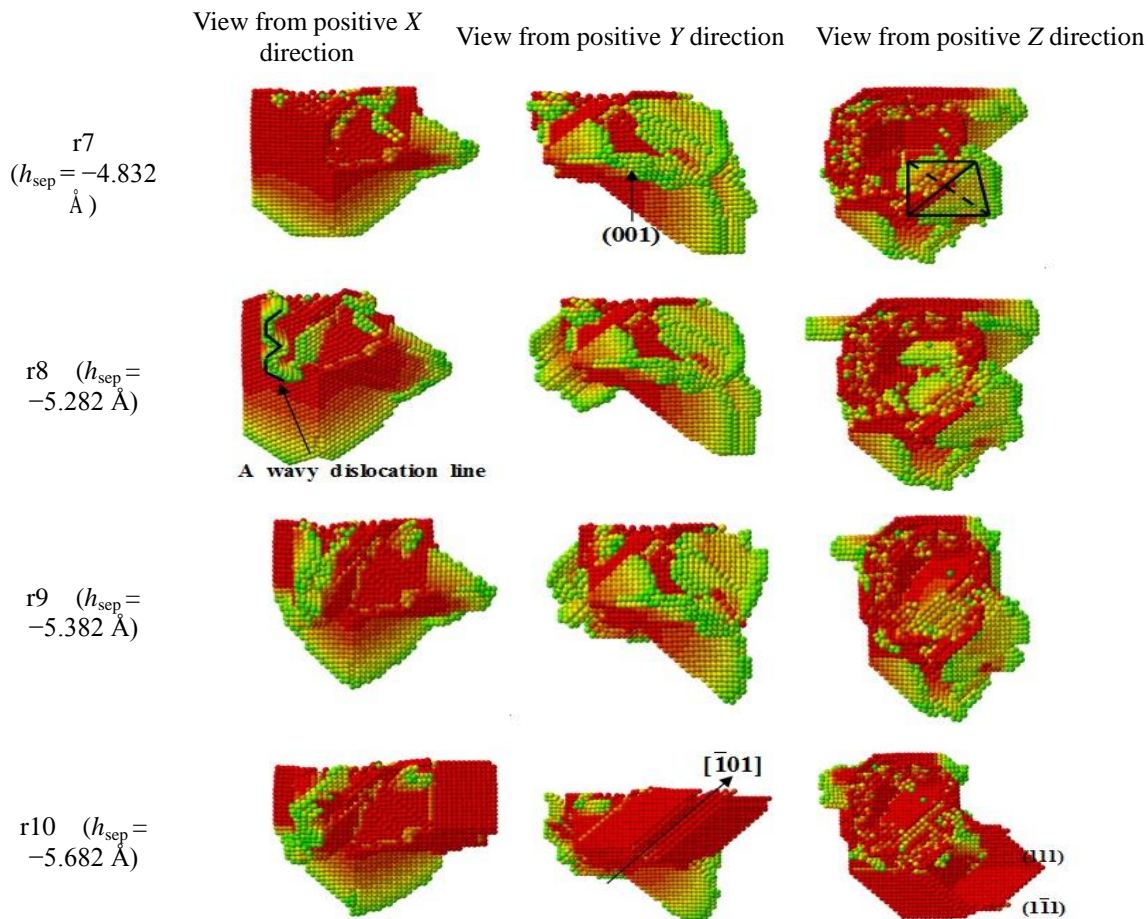


Fig. 12 Continued

### 3.3.3 Rectangular indenter

Three dislocation loops first nucleate from three out of the four corners (marked by three black circles in Fig. 12 at r1) of the rectangular indentation when the separation is equal to  $-1.082 \text{ \AA}$  (r1). As we can see in Fig. 12, atoms under the inactive corner exhibit large displacements, but do not develop into a dislocation loop until the separation reaches  $-3.182 \text{ \AA}$  (r3). These three dislocation loops continue to grow and interact with each other to form dislocation locks: lock 1 and lock 2 marked at r2 in Fig. 12. After these two locks appear, the material sample is hardened and the load-displacement curve begins to rise again until a large load drop occurs at r3.

At r3, the dislocation structure undergoes a dramatic change. A new dislocation loop appears at the originally inactive corner and interacts with the other dislocation loops to form new dislocation locks. We also observe dislocations that bow out from the already-formed dislocation locks, as denoted at r3 in Fig. 12. At r4, the dislocation structure does not change significantly, but the size is much larger.

At r5, a double cross-slip event is observed. The screw part of the dislocation loop originally on the  $(1\bar{1}\bar{1})$  plane cross-slips to the  $(111)$  plane, and then cross-slips back to the  $(1\bar{1}\bar{1})$  plane.

At r6, three cross-slip events are observed. The dislocation loop originally on the  $(1\bar{1}1)$  plane cross-slips to the  $(111)$  plane, and then back to the  $(1\bar{1}1)$  plane, before finally cross-slipping to the  $(111)$  plane, as denoted at r6 in Fig. 12.

At r7, the dislocation structure undergoes another dramatic transition. A cross-slip event is observed near one of the corners of the rectangular indenter. The dislocation loop cross-slips from the  $(111)$  plane to the  $(1\bar{1}\bar{1})$  plane and interacts with other dislocation loops to form a tetrahedral dislocation structure. This tetrahedral dislocation structure is bounded by the  $(1\bar{1}\bar{1})$ ,  $(11\bar{1})$ ,  $(1\bar{1}\bar{1})$ , and  $(11\bar{1})$  planes. This tetrahedral dislocation structure was also reported by Liang *et al.* (2004), who found that stress concentrates around this structure. This stress concentration phenomenon explains why some dislocation loops are observed to nucleate on the  $(001)$  plane, which is not a favored slip plane in FCC metals.

From r8 to r9, the dislocation structure does not change significantly, but a wavy dislocation line is observed, as noted at r8 in Fig. 12. At r10, a prismatic dislocation loop originating from inside the material sample glides upward to interact with the surface and form a mesa with a height of approximately  $1.814 \text{ \AA}$ . It also leaves a trace on the  $(111)$  and  $(1\bar{1}\bar{1})$  planes. The simulation finally terminates at  $h_{\text{sep}} \approx -6.182 \text{ \AA}$ . Compared to the dislocation activities of the other two cases, dislocation activities in the rectangular indenter case are far more complicated, and more complex dislocation interactions can be observed.

#### 4. Conclusions

We studied the influence of spherical, rectangular, and Berkovich indenters on nanoindentation into Al(001) using static molecular dynamics simulations. The elastic behavior for the three cases was well predicted by elastic contact theory. However, a noticeable discrepancy between the theoretical and simulated results in the Berkovich indenter case was found when the indentation depth was large. We concluded that the insufficient equivalence between the rigid conical indenter and the rigid Berkovich indenter was responsible for this deviation.

In all three cases, dislocation loops were mainly observed to nucleate on the  $\{111\}$  planes; this observation in accordance with the predictions of dislocation theory. In the rectangular indenter case, we observed that dislocation loops nucleated on the  $(001)$ , which is an unusual event in a face-centered cubic metal. We suggested that the complicated stress field generated by the rectangular indenter is responsible for this phenomenon. In the Berkovich indenter case, an amorphous region directly below the indenter tip was observed. We suggested that the extremely singular stress field around the indenter tip contributes to this uncommon observation.

Load drop events accompanied by transitions of the dislocation defect structure were found in all three cases. In the spherical indenter case, a twofold rotation-symmetric dislocation structure first nucleated, and then a prismatic dislocation loop originating from the surface appeared and glided downward out of the simulated cell. One significant and two smaller load drops occurred during the indentation. In the rectangular indenter case, dislocation activity was found to be prolific. Several significant load drop events accompanied by major transitions of the defect structure were observed. The dislocation structure became increasingly complicated as the indentation depth increased. We even observed a prismatic loop originating from inside the material sample gliding upward to create a mesa on the indenting surface. In addition, an unusual softening phenomenon was observed, and heterogeneously nucleating dislocations were suggested to be responsible for this. In the Berkovich indenter case, dislocation activities were moderate.

Load drops were observed to be small, and the defect structure did not change significantly. According to these results, we suggest that the shapes of indenters have different and significant influences on dislocation processes.

## Acknowledgements

Computational resources were provided by the National Center for High-Performance Computing and National Taiwan University. This research was supported by funding from the National Science Council of Taiwan (NSC 100-2628-E-002-035-MY3, NSC 100-2628-E-002-004, NSC 100-2627-E-002-001) and National Taiwan University (10R80920-05).

## References

- Bosakov, S.V. (2003), "Solving the contact problem for a rectangular die on an elastic foundation", *Int. Appl. Mech.*, **39**(10), 1188-1192.
- Chan, C.Y., Chen, Y.Y., Chang, S.W. and Chen, C.S. (2011), "Atomistic studies of nanohardness size effects", *Int. J. Theor. Appl. Multiscale Mech.*, **2**(1), 62-71.
- Chen, C.S., Wang, C.K. and Chang, S.W. (2008), "Atomistic simulation and investigation of nanoindentation, Contact Pressure and Nanohardness", *Interact. Multiscale Mech.*, **1**(4), 411-422.
- Ercolessi, F. and Adams, J.B. (1994), "Interatomic potential from first-principles calculations: the force-matching method", *Europhysics Lett.* **26**, 583-588.
- Fischer-Cripps, A.C. (2011), *Nanoindentation*, 3<sup>rd</sup> edition, Springer-Verlag, New York, USA.
- Hirth, J.P. and Lothe, J. (1982), *Theory of Dislocations*, 2<sup>nd</sup> edition, John Wiley & Sons, USA.
- Hosford, W.F. (1993), *The Mechanics of Crystals and Textured Polycrystals*, Oxford University Press, New York, USA.
- Kiely, J.D. and Houston, J.E. (1998), "Nanomechanical properties of Au (111), (001), (110) surface", *Phys. Rev. B*, **57**, 12588.
- Lee, Y., Park, J.Y., Kim, S.Y., Jun, S. and Im, S. (2005), "Atomistic simulations of incipient plasticity under Al(111) nanoindentation", *Mech. Mater.*, **37**, 1035-1048.
- Li, J., Vliet, K.J. Van, Zhu, T., Yip, S. and Suresh, S. (2002), "Atomistic mechanism governing elastic limit and incipient plasticity in crystals", *Nature*, **418**, 307-310.
- Liang, H.Y., Woo, C.H., Huang Hanchen, Ngan, A.H.W. and Yu, T.X. (2003), "Dislocation nucleation in the initial stage during nanoindentation", *Philos. Mag.*, **83**, 3609-3622.
- Liang, H., Woo, C.H., Huang, H., Ngan, A.H.W. and Yu, T.X. (2004), "Crystalline plasticity on copper (001), (110), and (111) surfaces during nanoindentation", *Comput. Model. Eng. Sci.*, **6**(1), 105-114.
- Lilleodden, E.T., Zimmerman, J.A., Foiles, S.M. and Nix, W.D. (2003), "Atomistic simulations of elastic deformation and dislocation nucleation during nanoindentation", *J. Mech. Phys. Solids*, **51**, 901-920.
- Press, W.H., Vetterling, W.T., Teukolsky, S.A. and Flannery, B.P. (2000), *Numerical recipes in C++: The Art of Scientific Computing*, Cambridge University Press, Cambridge. UK.
- Tadmor, E.B. and Miller, R.E. (2011), *Modeling Materials: Continuum, Atomistic and Multiscale Techniques*, Cambridge University Press.
- Vliet, K.J.V., Li, J., Zhu, T., Yip, S. and Suresh, S. (2003), "Quantifying the early stages of plasticity through nanoscale experiments and simulations", *Phys. Rev. B*, **67**, 104105.
- Zimmerman, J.A., Kelchner, C.L., Klein, P.A., Hamilton, J.C. and Foiles, S.M. (2001), "Surface step effects on nanoindentation", *Phys. Rev. Lett.*, **87**, 165507.